

## Biaxial test simulations using a packing of polygonal particles

A. A. Peña<sup>1,\*</sup>, A. Lizcano<sup>2</sup>, F. Alonso-Marroquin<sup>3</sup> and H. J. Herrmann<sup>4</sup>

<sup>1</sup>*Institute for Computational Physics, Pfaffenwaldring 27, Stuttgart 70569, Germany*

<sup>2</sup>*Universidad de los Andes, Bogotá D.C., Colombia*

<sup>3</sup>*Earth Systems Science Computational Centre, The University of Queensland, Sta. Lucia, Qld., Australia*

<sup>4</sup>*Institut für Baustoffe, ETH-Höenggerberg, Zürich, Switzerland*

### SUMMARY

The mechanical response of cohesionless granular materials under monotonic loading is studied by performing molecular dynamic simulations. The diversity of shapes of soil grains is modelled by using randomly generated convex polygons as granular particles. Results of the biaxial test obtained for dense and loose media show that samples achieve the same void ratio at large strains independent of their initial density state. This limit state resembles the so-called critical state of soil mechanics, except for some stress fluctuations, which remain for large deformations. These fluctuations are studied at the micro-mechanical level, by following the evolution of the co-ordination number, force chains and the fraction of the sliding contacts of the sample. Copyright © 2007 John Wiley & Sons, Ltd.

Received 25 October 2006; Revised 29 January 2007; Accepted 6 March 2007

KEY WORDS: granular material; biaxial test; critical state; interparticle friction; force fluctuations

### 1. INTRODUCTION

The stress–strain response of granular materials shows an incrementally nonlinear behaviour [1–3] when they are subjected to external loading. The macro-mechanical behaviour stems not only from phenomena occurring at the contact scale, but also from mesoscale arrangements such as fabric evolution [4] and force chains [5, 6].

\*Correspondence to: A. A. Peña, Institute for Computational Physics, Pfaffenwaldring 27, Stuttgart 70569, Germany.

†E-mail: andres@ica1.uni-stuttgart.de

Contract/grant sponsor: German-Israeli Foundation

Contract/grant sponsor: Deutsche Forschungsgemeinschaft; contract/grant number: HE 2732781

Contract/grant sponsor: EU project Degradation and Instabilities in Geomaterials with Application to Hazard Mitigation (DIGA)

Contract/grant sponsor: Australian Research Council

Contract/grant sponsor: Australian Computational Earth System Simulator

Contract/grant sponsor: Max-Planck Prize

Numerical simulations using the discrete element method (DEM) have become a valuable tool in the study of different phenomena occurring at the micro- and meso-mechanical scale in granular materials [7, 8]. The mechanical response of the media is obtained by modelling the particle interactions as a dynamic process and using simple mechanical laws in these interactions. Generally, discrete models use discs or spheres to reduce the time of calculation; however, this kind of models does not consider the effect of particle shape on the mechanical behaviour. Several researchers have studied this influence. Experimentally, Holubec and D'Appolonia [9] using fine to medium sand concluded that the variation order of the mechanical properties due to the shape of the particle, could be of the same magnitude as the variation due to the changes in density. By means of numerical simulations with DEM, Mirghasemi *et al.* [10] demonstrated that the particle angularity has an important effect in the compressibility and shear strength of the granular media. Matuttis [11] studied the effect of particle shape on the stress distribution in heaps of granular media. Matsushima and Saomoto [12] presented a method to construct irregularly shaped grains based on images of real granular material. Nougquier-Lehon *et al.* [13] studied in biaxial test simulations the influence of particle shape on the so-called critical state. Alonso-Marroquin *et al.* [14] show also that angularity significantly affect the force distribution inside the granular media, and hence the elasto-plastic response of the materials. The influence of irregular shape of polygonal particles on the structural changes in granular material has also been investigated using simulations of biaxial [15] and shear-cell [16] tests. It is therefore very important to take into account the particle shape in order to have a more realistic soil representation.

Force fluctuations under quasi-static loading is another aspect that is affected by particle shape. They appear as a consequence of frictional instabilities. Fluctuations are observed in glass bead samples [17] and packings of glass spheres [18]. Experimental biaxial tests show evidence of *dynamic instabilities* at the critical state [19]. Erratic slip-stick motion at the critical state is interesting, owing to its potential analogy with earthquake dynamics [20].

In this paper, molecular dynamics simulations of biaxial test are used to investigate the behaviour of granular materials under monotonic loading. We investigate stress fluctuations along with shear band formation, and also the dependency of the macroscopic friction on the contact friction. In order to include the effect of the diversity of shapes of a realistic soil, the grains are represented by randomly generated convex polygons. The overall behaviour is similar to the common observations in experiments and numerical simulations with circular particles. We show that the granular media evolve towards the critical state, where fluctuations of stress and abrupt collapse of the number of sliding contacts characterize the dynamic response.

The outline of this paper is as follows. The discrete model and the sample specifications are introduced in Section 2. In Section 3 we show that the biaxial test simulations reproduces the main features of the critical state in soil mechanics. The stress fluctuations and its correlation to the micro-mechanical variables is presented in Section 4. Finally, in Section 5 conclusions are exposed.

## 2. MODEL

The random generation of the convex polygons used in this model is carried out by means of a Voronoi tessellation. This is a simple method to discretize the media without introducing any kind of anisotropy [21]. The number of edges of the polygons is distributed between 4 and 8 for 98.7% of polygons (Figure 1).

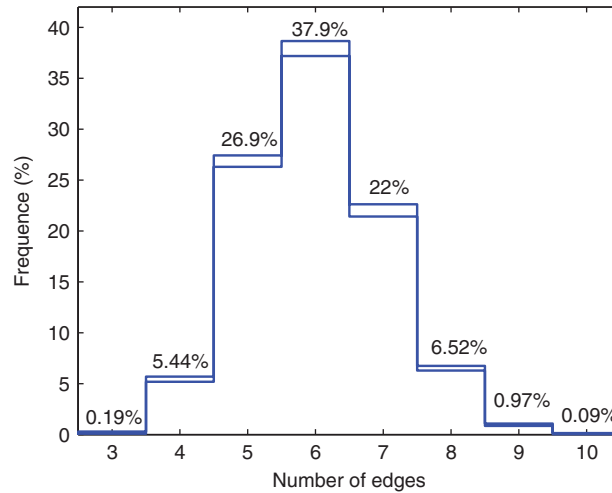


Figure 1. Distribution of number of edges. Five different generations, each one with 3600 polygons, were used in the calculations. The bars show the standard deviation of the data.

Once the sample has been created each particle is subjected to interparticle forces and boundary forces. It is assumed that particles interact elastically with each other. The polygons can neither be broken nor deformed, but they can overlap when they are pressed against each other. This overlap represents the local deformation of the grains. This approach has been thoroughly used to model many different processes, such as strain localization and earthquakes [8], fragmentation [22], and damage [23]. When all forces  $F_i$  acting on the particle  $i$ ,  $F^c$  from interparticle contacts and  $F^b$  from boundaries are known, the evolution of the position  $\mathbf{x}_i$  and orientation  $\theta_i$  of the  $i$  polygon is given by the integration of Newton's equation of motion:

$$-m_i \ddot{\mathbf{x}}_i + \sum_c \mathbf{F}_i^c + \sum_{c_b} \mathbf{F}_i^b = \mathbf{0} \quad (1)$$

$$-I_i \ddot{\theta}_i + \sum_c \mathbf{l}_i^c \times \mathbf{F}_i^c + \sum_{c_b} \mathbf{l}_i^b \times \mathbf{F}_i^b = \mathbf{0} \quad (2)$$

where  $m_i$  denotes the mass of particle  $i$ ,  $I_i$  its moment of inertia and  $\mathbf{l}$  the branch vector which connects the centre of mass of the polygon to the application point of the contact force. Each particle has two linear and one rotational degrees of freedom. In the following section the force laws are introduced.

### 2.1. Contact law

The contact force results from the overlap area  $a$  between particles. In Figure 2 the configuration of a particle contact is presented,  $P_1$  and  $P_2$  represent the intersection points between the edges of the polygons; the segment that connects those points gives the contact line  $\mathbf{S} = P_1 P_2$ . This vector defines a co-ordinate system at the contact ( $\hat{n}, \hat{t}$ ); where  $\hat{n}$  and  $\hat{t} = \mathbf{S}/|\mathbf{S}|$  normal to it give

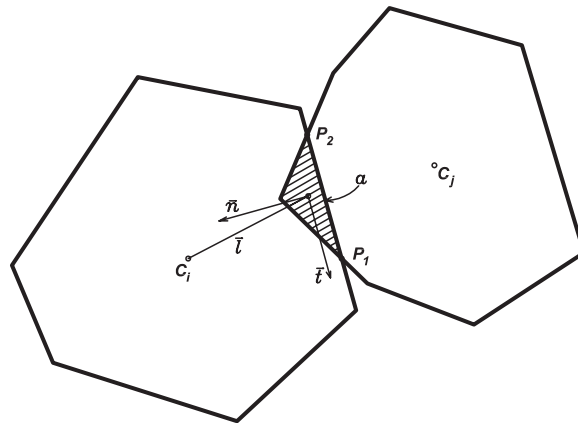


Figure 2. Schematic representation of a particle contact, the overlapping area  $a$  is indicated by the shaded zone.

the direction of the normal  $F_n$  and tangential  $F_t$  components of the contact force. The point of application of the contact forces is taken as the centre of mass of the overlap area [24].

The contact force is calculated as

$$\mathbf{F}^c = -k_n \delta \hat{n} - k_t \zeta \hat{t} \quad (3)$$

where  $k_n$  and  $k_t$  are the stiffnesses at the contact in the respective directions. The deformation length  $\delta$  is equal to  $a/|\mathbf{S}|$ . The tangential force is introduced by an elastic spring whose displacement  $\zeta$  is equal to 0 for new contacts, while for old contacts the tangential spring-length is obtained as follows:

$$\zeta = \zeta' + \mathbf{v}_t^c \Delta t_{\text{MD}} \quad (4)$$

where  $\zeta'$  is the previous length of the spring,  $\Delta t_{\text{MD}}$  is the time step of the molecular dynamic simulation, and  $\mathbf{v}_t^c$  the tangential component of the relative velocity  $\mathbf{v}^c$  at the contact

$$\mathbf{v}^c = \mathbf{v}_i - \mathbf{v}_j + \mathbf{w}_i \times \mathbf{l}_i - \mathbf{w}_j \times \mathbf{l}_j \quad (5)$$

Here,  $\mathbf{v}_i$  is the linear velocity and  $\mathbf{w}_i$  is the angular velocity of the particles in contact. The elastic tangential displacement  $\zeta$  at the contact increases until the Coulomb's sliding condition  $|F_t^c| = \mu F_n^c$  is reached. Here, the sliding condition is enforced keeping constant the tangential force. Finally, we introduce a viscous force (Equation (6)), which is necessary to maintain the numerical stability of the method and to obtain a quick convergence to the equilibrium configuration

$$\mathbf{F}_v^c = -m(v_n \cdot \mathbf{v}_n^c \cdot \hat{n}^c + v_t \cdot \mathbf{v}_t^c \cdot \hat{t}^c) \quad (6)$$

where  $m = (1/m_i + 1/m_j)^{-1}$  is the effective mass of the two particles in contact, and  $v_n$  and  $v_t$  are the damping coefficients. This damping force leads to velocity-independent normal and tangential restitution coefficients. These coefficients of restitution are given by the ratio between the relative

Table I. Parameters used in the model.

Parameter	Ratio	Value
Friction coefficient	$\mu$	0.55
Normal stiffness	$k_n$	$1.6 \times 10^8$ N/m
Normal damping coefficient	$v_n$	$4000$ s <sup>-1</sup>
Stiffness ratio	$\zeta = k_t/k_n$	0.33
Viscosity ratio	$v_t/v_n$	0.33
Time ratio	$t_0/t_s$	1000
Time step	$\Delta t_{MD}$	$2.5 \times 10^{-6}$ s

velocity before and after the collision. In particular, the normal restitution coefficient  $\varepsilon_n$  and  $v_n$  are related by the following expression [8]:

$$\varepsilon_n = \exp\left(\frac{-\pi v_n}{\sqrt{\omega_n^2 - v_n^2}}\right) \quad (7)$$

where  $\omega_n = \sqrt{k_n/m_0}$ , and here  $m_0$  is the mean mass of the polygons. Using the parameters of Table I, we obtain a value of  $\varepsilon_n$  equal to 0.73. This relatively low dissipation allows us to reduce viscous effects during loading.

## 2.2. Boundary conditions

During the simulation, the granular sample is confined by four rigid walls. These walls always maintain their horizontal or vertical orientation. Boundary forces are applied on each grain in contact with these walls. The walls are frictionless, so they transmit only normal forces to the polygons in contact with them. When one of the vertices of a polygon penetrates one of the walls, a force, proportional to the penetration length  $\delta$ , is applied on the polygon. This boundary force  $\mathbf{F}_n^b$  is oriented in normal direction  $\hat{n}$  to the wall (8)

$$\mathbf{F}_n^b = -k_n \delta \hat{n} \quad (8)$$

$$\mathbf{F}_v^b = -m_i v_n \mathbf{v}_n^c \quad (9)$$

Viscous forces  $\mathbf{F}_v^b$  in wall–polygons interactions are also considered (Equation (9)), where  $m_i$  is the mass of the particle in contact with the boundary wall, and  $v_n$  the damping coefficient in normal direction. The boundary force is calculated for all the cases of interaction between walls and polygons in the same way. Finally, the displacement of the walls and the total force on them are used to determine the global stress and strain of the assembly.

## 2.3. Parameters of the model

The parameters used in the model are presented in Table I. The interparticle friction coefficient was chosen  $\mu = 0.55$ , which yields similar values of macro-mechanic friction angles to those obtained in real materials as gravel or sands [25]. The stiffness ratio  $\zeta = k_t/k_n$  as well as the viscosity ratio ( $v_t/v_n$ ) were taken 0.33. The normal stiffness  $k_n$  was taken  $1.6 \times 10^8$  N/m; and the normal damping

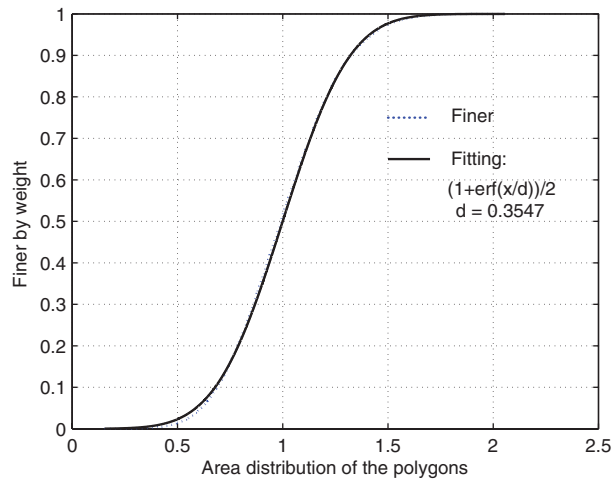


Figure 3. Cumulative distribution of polygon areas. The solid line shows the fit of the data using an error function. The distribution is calculated for  $1.8 \times 10^4$  polygons.

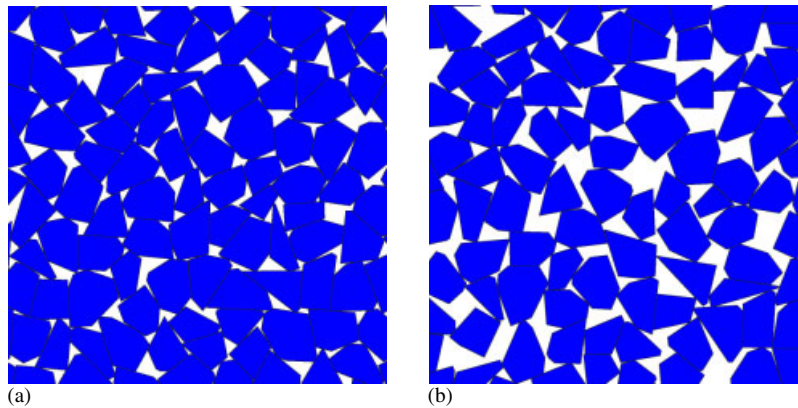


Figure 4. Sample configuration at the end of the construction process: (a) dense and (b) loose media.

coefficient  $\nu_n = 4000 \text{ s}^{-1}$ . The viscosity factors were selected to preserve numerical stability and to reduce the acoustic waves produced during loading. Finally, the time ratio in Table I is the ratio between the time of loading  $t_0$  and the characteristic period of oscillation  $t_s = \sqrt{m_0/k_n}$ . The value of  $t_s$  determines the selection of the time step  $\Delta t_{\text{MD}}$ . We use a 5th order predictor–corrector integration scheme, which preserve stability whenever  $\Delta t < 0.10 \times t_s$  [26].

#### 2.4. Sample construction

The distribution of areas of polygons is symmetric around its mean value  $1 \text{ cm}^2$ , and follows approximately a Gaussian distribution with variance of  $0.36 \text{ cm}^2$  (Figure 3). After generation of

the polygons, the sample is confined by applying a centripetal gravitational field to the particles and on the walls, oriented to the centre of mass of the assembly. Then the sample is compressed isotropically until the desired confining pressure is reached. In order to generate dense samples, the interparticle friction is set to zero during the construction. The loose samples are created taking damping coefficients 100 times greater than those used in the test stage. In both cases, the parameters are set to the values shown in Table I after the preparation of the sample. Figure 4 presents the sample configuration at the end of the construction process, for both dense and loose media. The sample specifications used to perform the simulations were: 1000 kg/m<sup>2</sup> for the density of particles, system size of 400 polygons, and a unitary shape ratio (width/height).

### 3. BIAXIAL TEST SIMULATIONS

In this test, the pressure in lateral walls  $\sigma_2$  is kept constant and the horizontal walls (axial direction) are moved at constant rate inducing deviatoric stress. The stress–strain behaviour at the macro-mechanical scale, for dense and loose systems, and its dependence on some mechanisms at the micro-mechanical scale are discussed. The effect of the interparticle coefficient of friction on the macro-mechanical response of the media is also studied.

In the test the axial and lateral directions are indicated as 1 and 2, respectively. That is  $\sigma_1$  and  $\varepsilon_1$  are the axial stress and strain, and  $\sigma_2$  and  $\varepsilon_2$  are the lateral components. The strains are defined as follows:

$$\varepsilon_1 = \frac{L_1^0 - L_1(t)}{L_1^0} \tag{10}$$

$$\varepsilon_2 = \frac{L_2^0 - L_2(t)}{L_2^0} \tag{11}$$

where  $L_1(t)$  and  $L_2(t)$  are the dimensions of the system at the time  $t$ , and  $L_1^0$  and  $L_2^0$  the dimensions at the beginning of the test. Stresses have the same sign convention used in soil mechanics: compressive normal stresses are positive and tensile normal stresses are negative.

The parameters used to perform the biaxial tests are presented in Table II.

#### 3.1. Macro-mechanical observations

Three different samples were used to evaluate the mechanical response of polygonal packings, each one corresponds to a different seed used in the random generation. The initial void ratios of the dense and loose samples are presented in Table III.

Table II. Parameters of the biaxial test.

Parameters	Value
Default confining pressure	160 kN/m
Axial strain rate	0.02 s <sup>-1</sup>
Maximum axial strain	20%

Table III. Initial void ratio of the samples.

Sample	Dense state	Loose state
1	0.128	0.251
2	0.130	0.262
3	0.135	0.271

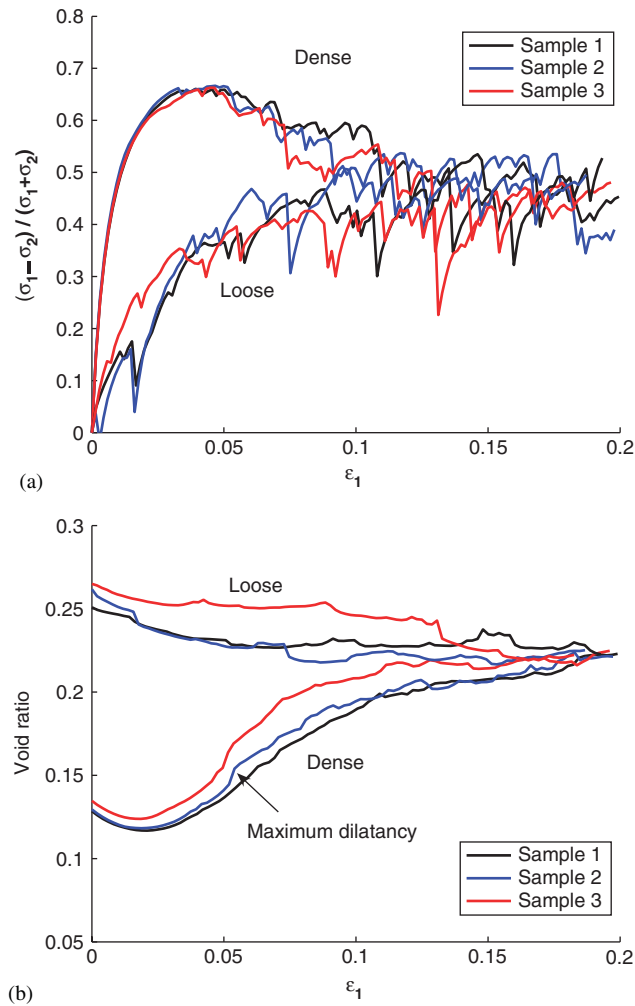


Figure 5. Evolution of (a) the deviator stress and (b) void ratio of the samples.

Figure 5(a) shows the evolution of  $\sin \phi = (\sigma_1 - \sigma_2) / (\sigma_1 + \sigma_2)$  with axial strain  $\varepsilon_1$  for the dense and loose system. In general, the dense samples exhibit a higher initial stiffness than the loose ones.

After the peak in the dense media, which is about 5% axial strain, a strain-softening behaviour is observed. The loose media exhibit more frequent and bigger variations in the stress behaviour. Additionally, a peak strength is not observed. Although an increase of fluctuations of the stress are observed for both systems at large deformations, it presents a tendency to stabilize around a value that one could consider as the steady state of the material ( $d \sin \phi / dt = 0$ ). The evolution of the void ratio with axial strain is illustrated in Figure 5(b). Initially, the dense samples contract and later the void ratio increases (dilatancy). For large axial strain values the void ratio reaches a constant value. Comparing the evolution of dense samples in Figure 5(a) and (b) we note that the maximum rate of dilatancy agrees with the peak strength (5% axial strain) which is expected on soils. It is especially observed in samples 2 and 3. The loose samples reduce their void ratio during the test (Figure 5(b)), and it tends to a constant ratio near to 18% axial strain. The void ratio in both dense and loose samples varies until it achieves the same value near to 0.23 corresponding to 18% axial strain. In this stage, the granular medium is deformed at constant volume and with the same approximate value of deviator stress, which corresponds to the critical state of the material and is independent of the initial sample density [27]. All these features reproduce the asymptotic behaviour of soils obtained in laboratory experiments [28].

*3.1.1. Shear bands.* Strain localization has been experimentally studied by several researchers in the last two decades, e.g. Vardoulakis [29], Desrues [30] and others. Using the DEM Cundall [31], and Bardet and Proubet [32] have studied this phenomenon. Theoretically, some authors have also investigated strain localization, for instance Vardoulakis [33], or Chambon *et al.* [34] by using the so-called second gradient method. In this paper, a brief analysis of strain localization is performed by studying the displacement of the individual particles. In Figure 6 the displacement vectors of the particles for the dense assembly are presented. At the beginning of the test, the displacements are very small and one can observe approximately a symmetrical deformation around the centre of the sample (Figure 6(a)). As the axial strain increases and before the peak strength is reached a slight tendency to strain localization is observed. After having overcome the peak strength, the particle displacements seem to define independent bodies with different displacement directions (a clearer strain localization). This localization persists as the loading increases, and becomes clearer around 8.9% axial strain (Figure 6(b)), where two ‘shear bands’ are observed. After peak, these shear bands are not constant in time. In fact, there are stages in which clear shear bands are observed, but they typically disappear, leading to a stress falloff. These falloffs, as we will see in Section 4, are related to force chains collapse and therefore to restructurations of the media that hinder the persistence of the shear bands. The particle displacements of Figure 6(a) and (b) are taken from two consecutive time intervals, which correspond to an increment of 0.1% of axial strain. Figure 6(c) presents the displacement at 20% axial strain measured from the particle initial position. Here, three bodies with different direction of displacement, and the areas (shear bands) defined between them are visible.

Although the particle displacements of loose samples are not shown, their evolution reflects the force chains collapse and consequent rearrangement of the particles within the sample. This is observed in the large displacements of the particles which are associated with the drops of the stress–strain behaviour [35]. Strain localization is not clear in loose media.

Concerning shear band orientation, most of the experimental data from biaxial tests on sand report that this orientation lies between the Mohr–Coulomb solution  $\theta_C = 45^\circ + \varphi/2$  and the Roscoe solution  $\theta_R = 45^\circ + \Psi/2$  [36]. The latter is defined by the angle of dilatancy  $\Psi = \arcsin(d\varepsilon_V/d\gamma)$ , being  $d\varepsilon_V$  and  $d\gamma$  the increments of volumetric and deviatoric strains at failure [37]. We observe

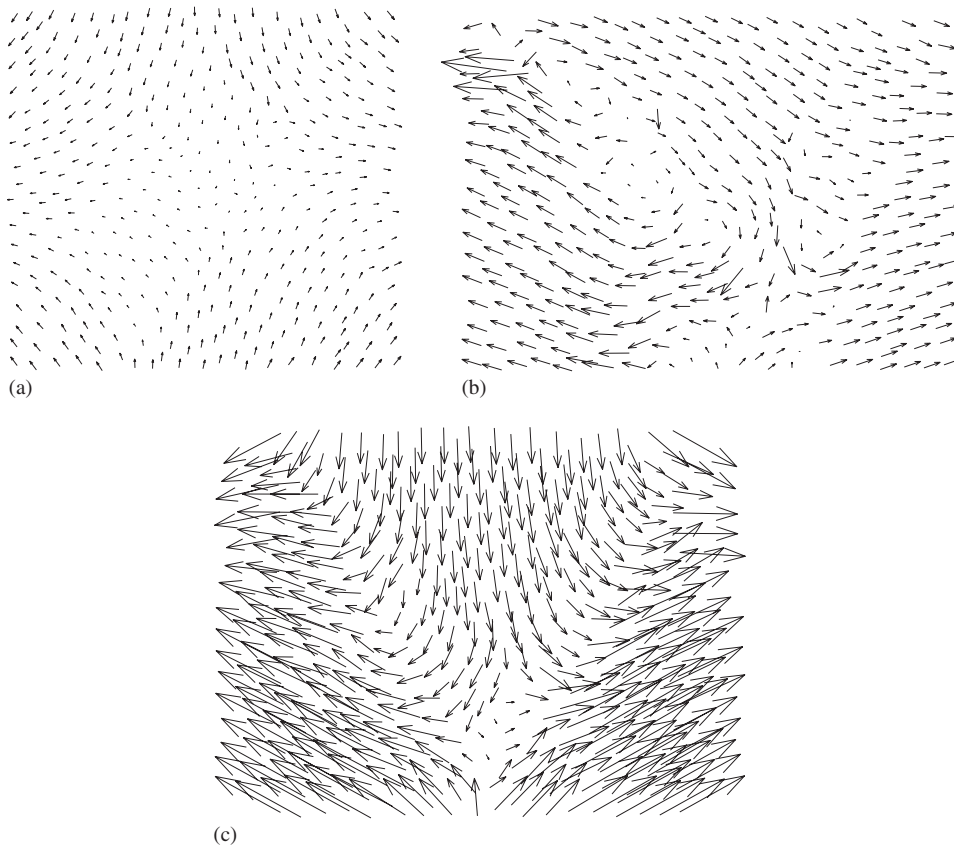


Figure 6. Displacement of particle centres within a dense sample at three axial strains: (a) 1.2%; (b) 8.9%; and (c) 20% of total.

that the inclination angle of the shear bands in Figure 6(c) are approximately between  $52$  and  $58^\circ$ . In this case, for  $\phi_{\text{micro}} = 28.8^\circ$  (Figure 8)  $\varphi \approx 26^\circ$  and  $\Psi \approx 15^\circ$  the predictions of Mohr–Coulomb and Roscoe solution define with very good agreement the limits for the angles found in the simulation.

*3.1.2. Macroscopic friction.* An approach to connect the Coulomb friction at the grain level to the macro-mechanical friction is to construct the Mohr–Coulomb failure surface of the granular sample. This failure surface can be obtained from the envelope of the Mohr circles at the peak stress value from biaxial tests [36]. The tests were carried out on dense samples, at three confining pressures: 80, 160 and 320 kN/m. Different methods are used to describe the failure surface of granular soils. In the following analysis, as used in traditional soil mechanics, we assumed that the failure surface is linear. Figure 7 shows the failure envelope of a granular sample with interparticle friction coefficient  $\mu = 0.55$  that corresponds to an interparticle friction angle  $\phi_{\text{micro}}$  of  $28.8^\circ$  ( $\mu = \tan \phi$ ). The envelope is plotted as a tangent straight line to the Mohr circles, and the angle of friction of the bulk material is approximately  $41^\circ$ . In our simulations, the macroscopic angle of

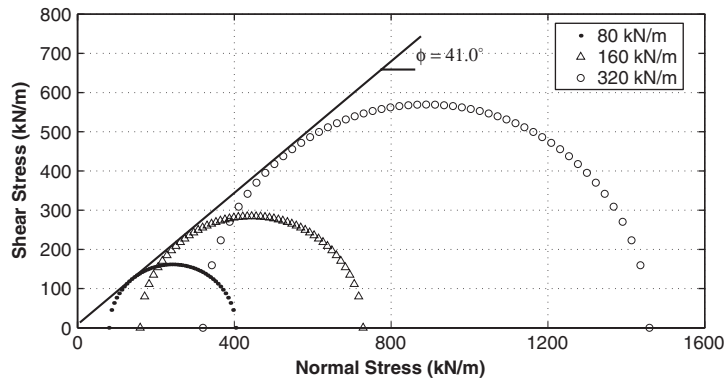


Figure 7. Mohr–Coulomb failure envelope constructed from biaxial test and Mohr circles. Interparticle friction angle  $\phi_{\text{micro}} = 28.8^\circ$ .

friction was found to be independent of system sizes varying from 100 to 2000 particles. Larger system sizes were not used.<sup>‡</sup>

If we compare this result with the one obtained by Bardet using DEM with disks [38], we can then observe the important influence of particle shape on the macro-mechanical angle  $\phi_{\text{peak}}$  of the medium. For instance, using very similar values of  $\phi_{\text{micro}}$ ,  $28.8^\circ$  for polygons and  $26.5^\circ$  for disks, the obtained values of  $\phi_{\text{peak}}$  are  $41^\circ$  and  $22^\circ$ , respectively. The ratio  $\phi_{\text{peak}}/\phi_{\text{micro}}$  is then equal to 1.42 for polygons and 0.83 for disks. Furthermore, as mentioned in the previous section, different macro-mechanical angles are correlated to different orientations of strain localization (shear band). In the case of disks, if particle rotation is constrained, as in Reference [38], a value of  $\phi_{\text{peak}} = 41^\circ$  is obtained. In such case, although  $\phi_{\text{peak}}$  is equal to the value for polygons, the sample dilatancy is almost completely hindered and therefore the stress–strain behaviour of the sample is highly affected. For example, no correlation between peak strength and maximum rate of dilatancy is observed. All these observations confirm the important role of particle shape on the global behaviour of granular media.

In order to study the effect of the interparticle friction  $\phi_{\text{micro}}$  on the macro-mechanical friction angle  $\phi_{\text{macro}}$ , different interparticle friction coefficients and five different samples were used in the simulations. Additional to the friction angle at the peak stress  $\phi_{\text{peak}}$ , the friction angle at the critical state  $\phi_{\text{critic}}$  was also calculated. Figure 8 shows for the five samples the values of  $\phi_{\text{peak}}$  and  $\phi_{\text{critic}}$  obtained from variations of  $\phi_{\text{micro}}$ . It is observed that at very low values of  $\phi_{\text{micro}}$  the macro-mechanical angles are quite similar. For values of interparticle friction angle larger than  $15^\circ$  the granular samples develop a clear peak strength  $\phi_{\text{peak}}$  (value different from  $\phi_{\text{critic}}$ ), while the  $\phi_{\text{critic}}$  value remains approximately constant. The last agrees with the experimental results obtained by Skinner [39], excluding the results from micro-mechanical angle close to zero. These results suggest that, except at small values of  $\phi_{\text{micro}}$  where microscopic friction plays an important role, the friction angle mobilized at the critical state  $\phi_{\text{critic}}$  is independent of the interparticle friction coefficient. This particular feature has been also observed in numerical simulations with circular

<sup>‡</sup>Simulations of much larger number of particles are limited by the architecture of the programme, which requires static storage allocation for all variables.

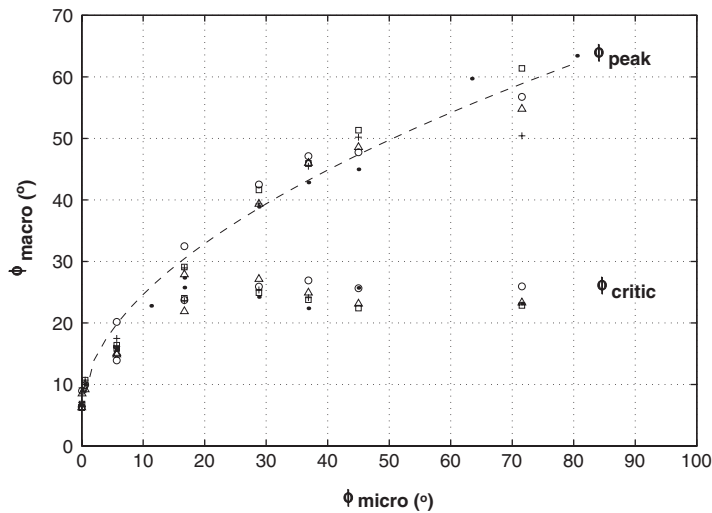


Figure 8. Macro-mechanical friction angle at peak and at critical state. The dashed line is a power law approximation  $\phi_{\text{peak}} = 5.5 \cdot \phi_{\text{micro}}^{0.53} + 6$ .

particles [20]. The non-dependence of macroscopic friction on contact friction is attributed to the spontaneous formation of rotational patterns, such as the vorticity field shown in the part (b) of Figure 6, and clusters of particles with intense rolling. Those deformation modes have been seen to reduce considerably the bulk friction with respect to the expected value of the simple shear deformation [20].

Note that setting  $\phi_{\text{micro}}$  to zero, a value of  $\phi_{\text{macro}}$  close to 6.0 is obtained. Although this value of  $\phi_{\text{macro}}$  is calculated from the average of the deviator stress, the frictionless granular media offer a resistance to shear. Similar results have been found experimentally by Skinner [39], in theoretical work by Cambou [40], and more recently in DEM using disks by Krut [41]. This supports the idea that interparticle friction is not the unique cause of the macroscopic frictional behaviour of granular materials, in fact, it might be certainly a consequence of the non-local behaviour of granular assemblies where the contact scale is not the basic constitutive element.

#### 4. STRESS FLUCTUATIONS

According to the critical state soil mechanics, large shear deformations drive the granular specimen to limiting state. This state is characterized by an isochoric deformation, where the stress ratio and the frictional dissipation stay constant [28]. This is not exactly what our simulations show. Indeed, we find that samples with different densities reach the same critical state, where the density and the stress ratio stay approximately constant, except for some fluctuations. In this section we investigate the onset of such instabilities exploring the time evolution of the microstructural variables. The simplest way to explore micro-structural arrangement of the granular sample is by following the evolutions of the following two internal variables: (1) the co-ordination number and, (2) the fraction of sliding contact.

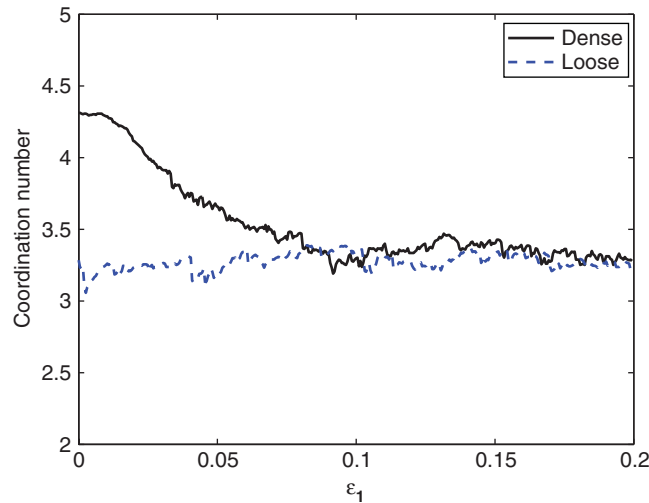


Figure 9. Evolution of the average co-ordination number during the biaxial test.

The co-ordination number  $Z$  is defined as the average of the number of contacts per particle. The evolution of the co-ordination number of one of the samples is presented in Figure 9. In our model, edge-to-edge contact, as well as edge-to-vertex contact, are treated in the same way as explained in Section 2.1. At low axial strain values, the dense system contracts and as a consequence a small increment of  $Z$  is observed. This is followed by a decrease of the  $Z$  value when the system dilates. This decrease is associated with the formation of force chains along the direction of loading and the breaking of interlocking between particles. As a result, each particle begins to lose contacts. This is macro-mechanically observed by the trend of dense samples to increase their volume. In contrast, the loose granular sample tends to a denser structure, and therefore new contacts are generated. Both samples around 8% axial strain reach a co-ordination number  $Z$  close to 3.3. Here, the media are highly susceptible to collapse.

In Figure 10 the direct relation between stress drops and collapse of force chains is presented. We selected one of the several stress drops as depicted in Figure 10(a). Then we plot the contact forces of the particles just before the stress drop Figure 10(b) and right after it Figure 10(c). Comparing these two force networks, one can see that some of the principal force chains after the stress drop have collapsed and therefore disappeared. This collapse drives the system to an internal rearrangement, in which particles undergo big relative displacements. The last is confirmed by the study of the displacement field of the individual particles [35], where big displacements of the particles are associated with abrupt reductions of the stress. Between two collapses the force chains build up leading to an increase of the macroscopic friction coefficient.

The micro-structure of these collapses can be also visualized in the population of the sliding contacts. Figure 11 shows the evolution of the ratio between the number of sliding contacts and the total number of contacts. The sliding condition is given by the Coulomb's condition,  $F_t^c = \mu \cdot F_n^c$ . Initially, the dense medium has more sliding contacts when it contracts. Later when the sample begins to expand the number decreases. In general, the evolution of the sliding contacts for both systems during loading, consists of stages where their number increases, and short time 'failures' where the fraction of sliding contacts jumps down.

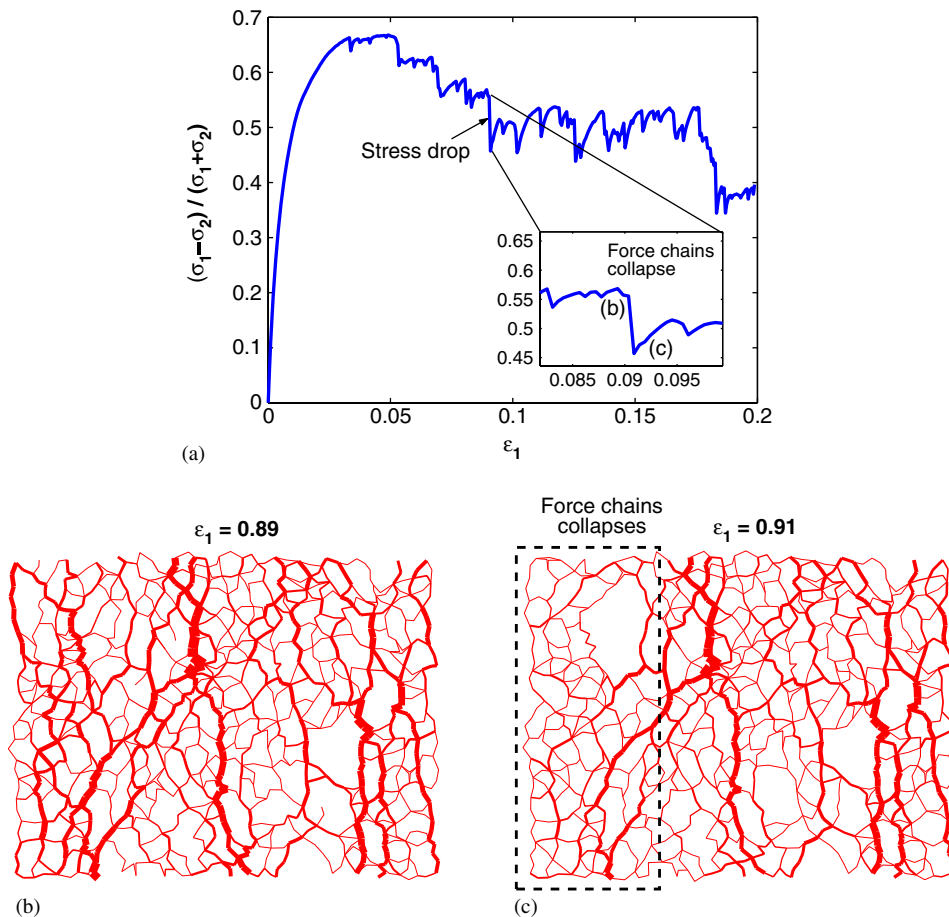


Figure 10. Stress drops (a) and their correlation with collapse of force chains: force network just before the stress drop (b) and right after it (c). The width of the lines is proportional to the magnitude of the contact force. The spatial correlation of the contact network in a packing of polygons is more pronounced than in the case of disks. This is reflected in the exponential tail of the distribution of contact forces. In the case of polygons, it is given by  $N(f_n) \sim \exp(-x^{1.6})$  [42]. This is different from the distribution  $N(f_n) \sim \exp(-x)$  of circular particles [43].

Figure 12 compares the stress–strain evolution to the fraction of sliding contacts for the dense and loose sample. We observe more initial stability, with low frequency of jumps in the stress, in the dense sample. This stability is related to the average co-ordination number of the medium (Figure 9), and the bigger this value the bigger the resulting stability of the granular skeleton. Although the jumps observed in the stress–strain behaviour are less frequent than ones in the sliding contacts (Figure 12), each stress jump is associated with an abrupt reduction of the number of sliding contacts. Each stress drop matches with a collapse of the fraction of sliding contacts.

These jumps in the stress deviator are present in realistic experiments of granular soils, but on a smaller scale [17, 18]. In our simulations the magnitude of these fluctuations can be partially

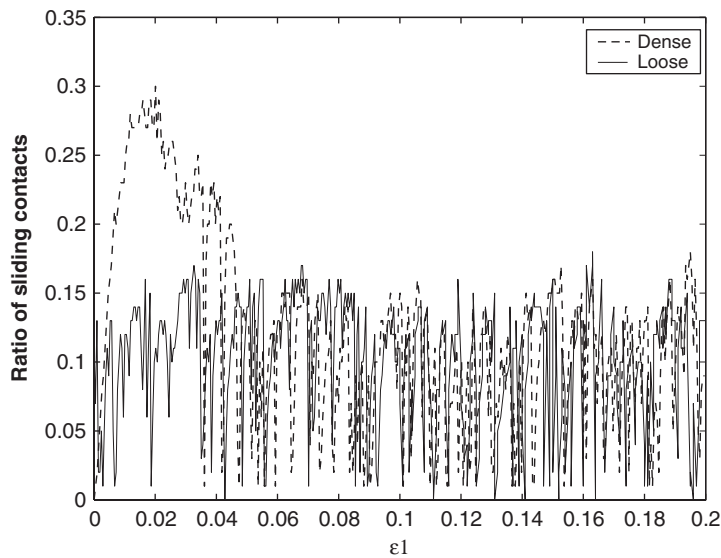


Figure 11. Evolution of the fraction of sliding contacts ratio during the biaxial test.

attributed to the small size of the sample. One may ask the question if these fluctuations disappear as the size of the sample increases. Previous numerical simulations with the same model show that these fluctuations barely decrease as the number of particles of the specimen increases [44]. The distribution of energy released of these fluctuations in shear cell experiments follows approximately a power law [8]. The analogy of this statistics with the Gutenberg–Richter law suggests us that a detailed investigation of the collapse of force chains will improve our understanding of earthquakes.

## 5. DISCUSSION AND FINAL REMARKS

In this paper the effect of the initial density of the sample and the interparticle coefficient of friction on the macro-mechanical behaviour of granular materials was investigated. The results show that at large strains the samples reach the critical state independent on their initial density, and they deform at constant void ratio, volume and mechanical co-ordination number. We have proven that for a wide range of contact friction coefficients, axial loading leads to the same critical state. In this state the system approaches and retreats an unstable behaviour leading to strong fluctuations of stress.

The stress drops were correlated to the evolution of the co-ordination number and the fraction of sliding contacts. We found that the granular sample at critical state develop force chains highly susceptible to collapse, driven to strong stress fluctuations. Stress collapses remove the contacts from the sliding condition, and therefore lead to a temporal stability in the granular sample. Can the stick–slip fluctuations in granular media be characterized by such natural tendency of the system to build up force chains susceptible to collapse under large shear deformations?. To answer this question we require a systematic study of the geometrical properties of the contact network. Current geometrical characterization of force chains has been done for two-dimensional packing

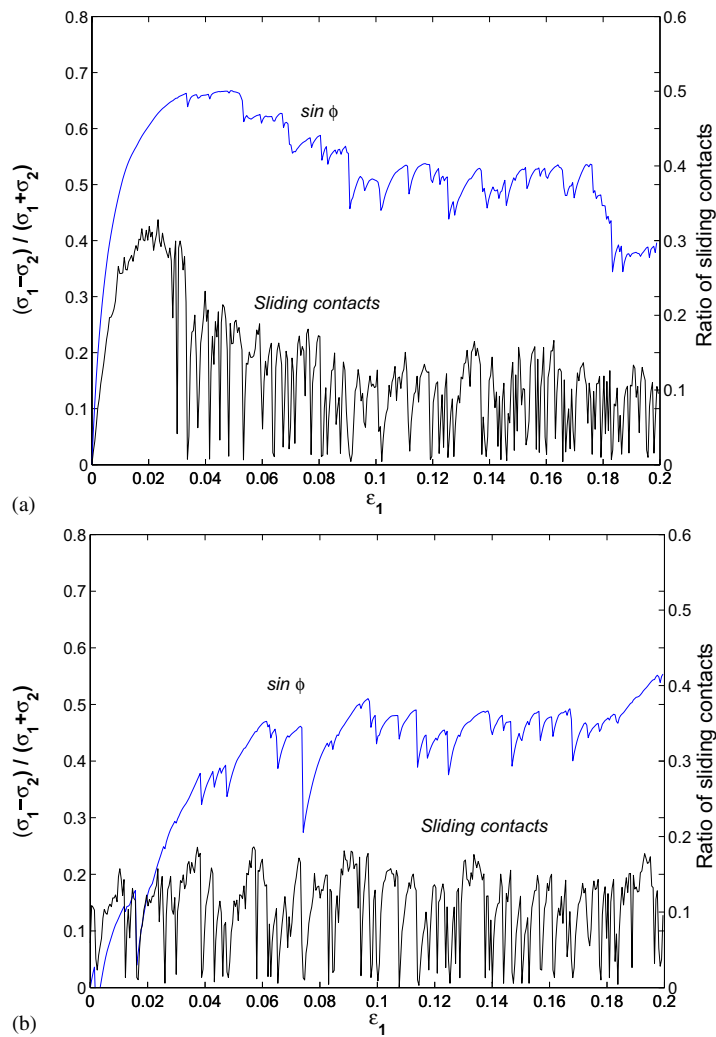


Figure 12. Evolution of stress and the fraction of sliding contacts with axial strain: (a) dense and (b) loose samples.

of disks [45]. The extension of this method for complex shaped particles and its application to monotonic shear deformations will potentially explain the nature of the stick–slip fluctuation on sheared granular materials.

#### ACKNOWLEDGEMENTS

The authors want to acknowledge the support of the German-Israeli Foundation (GIF), the *Deutsche Forschungsgemeinschaft* Project HE 2732781 *Micromechanische Untersuchung des granulares Ratchetings*, and the EU project Degradation and Instabilities in Geomaterials with Application to Hazard

Mitigation (DIGA) in the framework of the Human Potential Program, Research Training Networks (HPRN-CT-2002-00220). Alonso-Marroquin acknowledges the support of the Australian Research Council and the Australian Computational Earth System Simulator. Hans Herrmann acknowledges the Max-Planck Prize.

## REFERENCES

1. Darve F. The expression of rheological laws in incremental form and the main classes of constitutive equations. In *Fractured and Jointed Rock Masses*, Darve F (ed.). Taylor & Francis: London, 1990; 123–148.
2. Bardet JP. Numerical simulations of the incremental responses of idealized granular materials. *International Journal of Plasticity* 1994; **10**:879–908.
3. Darve F, Nicot F. On incremental non linearity in granular media: phenomenological and multiscale views (part i). *International Journal for Numerical and Analytical Methods in Geomechanics* 2005; **29**:1387–1409.
4. Nicot F, Darve F. A multiscale approach to granular materials. *Mechanics of Materials* 2005; **37**(9):980–1006.
5. Cates ME, Wittmer JP, Bouchaud JP, Claudin P. Jamming, force chains, and fragile matter. *Physical Review Letters* 1998; **81**(9):1841–1844.
6. Majmudar TS, Behringer RP. Contact force measurements and stress-induced anisotropy in granular materials. *Nature* 2005; **435**(23):1079–1082.
7. Cundall PA, Strack ODL. A discrete numerical model for granular assemblies. *Géotechnique* 1979; **29**(1):47–65.
8. Tillemans HJ, Herrmann HJ. Simulating deformations of granular solids under shear. *Physica A* 1995; **217**: 261–288.
9. Holubec I, D'Appolonia E. Effect of particle shape on the engineering properties of granular soils. *ASTM STP* 1973; **523**:304–318.
10. Mirghasemi A, Rothenburg L, Matyas E. Influence of particle shape on engineering properties of assemblies of two-dimensional polygon-shaped particles. *Geotechnique* 2002; **52**:209–217.
11. Matuttis HG. Simulations of the pressure distribution under a two dimensional heap of polygonal particles. *Granular Matter* 1998; **1**(2):83–91.
12. Matsushima T, Saomoto H. Discrete element modeling for irregularly-shaped sand grains. In *Proceedings NUMGE2002: Numerical Methods in Geotechnical Engineering*, Mestat (ed.), Paris, 2002; 239–246.
13. Nouguier-Lehon C, Cambou B, Vincens E. Influence of particle shape and angularity on the behaviour of granular materials: a numerical analysis. *International Journal for Numerical and Analytical Methods in Geomechanics* 2003; **27**:1207–1226.
14. Alonso-Marroquin F, Luding S, Herrmann HJ, Vardoulakis I. Role of the anisotropy in the elastoplastic response of a polygonal packing. *Physical Review E* 2005; **51**:051304.
15. Nouguier-Lehon C, Vincens E, Cambou B. Structural changes in granular materials: the case of irregular polygonal particles. *International Journal of Solids and Structures* 2005; **42**:6356–6375.
16. Peña AA, García-Rojo R, Herrmann HJ. Influence of particle shape on sheared dense granular media. *Granular Matter* 2007, in press.
17. Nasuno S, Kudrolli A, Bank A, Gollub JP. Time-resolved studies of stick-slip friction in sheared granular layers. *Physical Review E* 1998; **58**(2):2161–2171.
18. Adjemian F, Evesque P, Jia X. Ultrasonic experiment coupled with triaxial test for micro-seismicity detection in granular media. In *Powders and Grains 2005*, García-Rojo R, Herrmann HJ, McNamara S (eds). Balkema: Stuttgart, Germany, 2005; 281–285.
19. Vardoulakis I, Georgopoulos IO. The stress-dilatancy hypothesis revisited: shear-banding related instabilities. *Soils and Foundations* 2005; **45**:61–76.
20. Alonso-Marroquin F, Vardoulakis I, Herrmann HJ, Weatherley D, Mora P. Effect of rolling on dissipation in fault gouges. *Physical Review E* 2006; **74**:031306.
21. Lauritsen KB, Moukarzel C, Herrmann HJ. Statistical laws and mechanics of voronoi random lattices. *Journal of Physique I* 1993; **3**:1941–1951.
22. Kun F, Herrmann HJ. Fragmentation of colliding discs. *International Journal of Modern Physics C* 1996; **7**(6):837–855.
23. Kun F, Herrmann HJ. Transition from damage to fragmentation in collision of solids. *Physical Review E* 1999; **59**(3):2623–2632.
24. Alonso-Marroquin F, Herrmann HJ. Calculation of the incremental stress-strain relation of a polygonal packing. *Physical Review E* 2002; **66**:021301.

25. Bardet JP. *Experimental Soil Mechanics*. Prentice-Hall: New Jersey, 1997.
26. Allen MP, Tildesley DJ. *Computer Simulation of Liquids*. Oxford University Press: Oxford, 1987.
27. Schofield AN, Wroth CP. *Critical State Soil Mechanics*. McGraw-Hill: New York, 1968.
28. Wood DM. *Soil Behaviour and Critical State Soil Mechanics*. Cambridge University Press: Cambridge, 1990. ISBN: 0-521-33782-8
29. Vardoulakis I. Shear band inclination and shear modulus of sand in biaxial tests. *International Journal for Numerical and Analytical Methods in Geomechanics* 1980; **4**:103–119.
30. Desrues J. Localization de la deformation plastique dans les materieux granulaires. *Ph.D. Thesis*, University of Grenoble, Grenoble, France, 1984.
31. Cundall PA. Numerical experiments on localization in frictional materials. *Ingenieur-Archiv* 1989; **59**:148–159.
32. Bardet JP, Proubet J. A numerical investigation of the structure of persistent shear bands in granular media. *Geotechnique* 1991; **41**(4):599–613.
33. Vardoulakis I. Shear-banding, liquefaction in granular materials on the basis of a Cosserat continuum theory. *Ingenieur-Archiv* 1989; **59**:106–113.
34. Chambon R, Caillerie R, Matsushima T. Plastic continuum with microstructure, local second gradient theories for geomaterials: localization studies. *International Journal of Solids and Structures* 2001; **38**:8503–8527.
35. Peña AA. Simulación numérica de la respuesta esfuerzo deformación de medios granulares no cohesivos. *M.Sc. Thesis*, Universidad de los Andes, Bogotá D.C., Colombia, 2004.
36. Vermeer PA. The orientation of shear bands in biaxial tests. *Géotechnique* 1990; **40**:223.
37. Roscoe FH. The influence of the strains in soil mechanics. *Geotechnique* 1970; **20**(2):129–170.
38. Bardet JP. Observations on the effects of particle rotations on the failure of idealized granular materials. *Mechanics of Materials* 1994; **18**:159–182.
39. Skinner A. A note on the influence of interparticle friction on the shearing strength of a random assembly of spherical particles. *Geotechnique* 1969; **19**(1):150–157.
40. Cambou B. From global to local variables in granular materials. In *Powders and Grains 93*, Thornton C (ed.). Balkema: Stuttgart, Germany, 1993; 73–86.
41. Krut NP, Rothenburg L. Strength, dilatancy, energy and dissipation in quasi-static deformation of granular materials. In *Powders and Grains 2005*, García-Rojo R, Herrmann HJ, McNamara S (eds). Balkema: Stuttgart, Germany, 2005; 251–255.
42. Alonso-Marroquin F. Micromechanical investigation of soil deformation: incremental response and granular ratcheting. *Ph.D. Thesis*, University of Stuttgart, Stuttgart, Germany, 2004.
43. Radjai F, Jean F, Moreau JJ, Roux S. Force distribution in dense two-dimensional granular systems. *Physical Review Letters* 1996; **77**(2):274.
44. García-Rojo R, McNamara S, Peña AA, Herrmann HJ. Sliding, localization in a biaxial test of granular material. In *Powders and Grains 2005*, García-Rojo R, Herrmann HJ, McNamara S (eds). Balkema: Stuttgart, Germany, 2005; 705–708.
45. Peters JF, Muthuswamy M, Wibowo J, Tordesillas A. Characterization of force chains in granular material. *Physical Review E* 2005; **72**:041307.